Data Sets for Hydrogen Reflection and their Use in Neutral Transport Calculations

W. Eckstein and D.B. Heifetz

IPP 9/59 August 1986

MAX-PLANCK-INSTITUT FÜR PLASMAPHYSIK

8046 GARCHING BEI MÜNCHEN

MAX-PLANCK-INSTITUT FÜR PLASMAPHYSIK

GARCHING BEI MÜNCHEN

Data Sets for Hydrogen Reflection and their Use in Neutral Transport Calculations

W. Eckstein and D.B. Heifetz

IPP 9/59 August 1986

Die nachstehende Arbeit wurde im Rahmen des Vertrages zwischen dem Max-Planck-Institut für Plasmaphysik und der Europäischen Atomgemeinschaft über die Zusammenarbeit auf dem Gebiete der Plasmaphysik durchgeführt.

DATA SETS FOR HYDROGEN REFLECTION AND THEIR USE IN NEUTRAL TRANSPORT CALCULATIONS

W. Eckstein
Max-Planck-Institut für Plasmaphysik
8046 Garching bei München
Euratom-Association
Federal Republic of Germany

D.B. Heifetz
Plasma Physics Laboratory, Princeton University
Princeton, N.J. 08544

Abstract

A realistic characterization of the interaction of ions and neutral particles with device walls is important for any edge plasma calculation. Present reflection models vary in detail and computational efficiency. This paper presents a data set for the distribution of the reflection coefficient, R_N, over reflected energy, polar, and azimuthal angles, as functions of incident polar angle and energy. These results have been computed using a vectorized version of the TRIM Monte Carlo code. The data are stored using an algorithm for reducing the data into three one-dimensional distributions, resulting in a realistic reflection model which can be used very efficiently in plasma edge calculations.

Keywords: Wall reflection, neutral transport.

1. Introduction

One main process in the recycling of hydrogen in controlled fusion devices is the kinetic reflection of hydrogen from the walls. Neutral transport codes describing the boundary plasma require a wall reflection model. Particles which do not reflect are sources for wall diffusion and desorption models.

Three approaches to wall reflection modeling in transport codes are possible:

1. Using simple energy and angle-dependent algebraic fits to experimental and computed data such as those found in Refs. 1-3. This approach is computationally fast but simplistic. A more detailed description of reflection which includes energy and angular distributions of reflected particles is of interest as input into transport codes, in particular in Monte Carlo algorithms, where complicated distributions can be easily incorporated. These reflection distributions have been measured at the higher energies [1] and computed with Monte Carlo programs [4,5]. Analytic treatments of neutral transport, however, do benefit from realistic approximations expressed in closed, algebraic form.

2. Using reflection simulation codes to create stored data sets of reflection coefficients and angular distributions. Necessary for including the large multidimensional tables that this approach requires is an efficient scheme for sampling the distributions. One drawback of this method is that statistical inaccuracies in the original data will be forever present in the data compilation.

3. Incorporating a reflection code, such as TRIM [5], directly into the transport code. This avoids the problem in approach 2 of embedded inaccuracies. An additional advantage is that the projectile species and wall structure can be easily varied. No new tables would have to be generated for each new projectile/target combination. The combined transport+wall reflection computations may, however, be costly to run (see Sec. 4). Besides adding the expense to the transport code of calculating the wall reflection process directly, extra calculations may be necessary to smooth out the extra statistical variations introduced into the calculation by the reflection code.

We describe in this paper our development of the second approach. An algorithm has been developed [6] which takes all reflection data into account, but reduces this data to a reasonable number of values. The MARLOWE program [4] was used to create a data set for use in the DEGAS neutral transport code [7]. The purpose of the present work is to use the TRIM program to extend the energy range of this data down to 1 eV, to include a carbon target together with the iron one, and to reduce the standard deviations of the results.

We discuss in Section 2 the data production program, a modified version of the TRIM code. Section 3 describes the data reduction method, and implementation of the algorithm in transport codes is discussed in Section 4.

2. The Data Production Program

The reflection data are produced with the Monte Carlo program NEWTRD, which is a vectorized version of the TRIM program [8]. The gain of computing speed was about a factor of four in comparison to the earlier TRIM version [9]. Another change was that

the usually fixed distance $\lambda = N^{-1/3}$, where N is the density of the target, between two collisions is reduced by τ, the so-called time-integral [10]. At energies below 50 eV, the Oen-Robinson local inelastic energy loss [11] was applied, whereas for incident energies $E_o \geq 50$ eV the Andersen-Ziegler values [12] for the nonlocal inelastic energy loss were used. The reason is that the Andersen-Ziegler energy loss gives energy losses greater than the elastic losses at low energies. A consequence of the Andersen-Ziegler loss is a multiple peak structure in the energy distributions of reflected particles, caused by the small number of collisions in the solid. The reflection coefficients differed only slightly between using the two inelastic energy models above 50 eV. The Kr-C potential [13] was used as the interaction potential to determine the scattering angle and the elastic energy loss. It has been shown that the Kr-C potential is a good mean interaction potential for all ion-target combinations [14].

The most important uncertainties in the calculation are due to the applied interatomic potential and inelastic energy loss models, the binary collision approximation at low energies, and the surface structure. The first three ones are discussed in Ref. 9. The measured data in the keV range also have an absolute uncertainty of about 20%, so that the agreement between experimental and calculated data limits the possible absolute accuracy of the calculated data.

The effect of surface roughness is difficult to characterize. Most surface structures will decrease the reflection coefficient [1,15,16], so that our calculated data for an atomically rough surface will be an upper limit. Also the energy and angular distributions may change with a different surface structure. Because of the practically unlimited possible surface structures in a plasma machine, and their dependence on time, it is nearly impossible to simulate the real rough surface in the computations.

One way to simulate roughness is to use the calculated reflection data for smooth surfaces together with a roughness factor, ε, equal to the number of additional reflections a particle would have to undergo before leaving the wall. This factor would increase with greater roughness. In a Monte Carlo algorithm, for example, a test flight would be tested for reflection ε times, making the effective reflection coefficient roughly equal to the measured one to the power ε. This model assumes that the particle does not lose so much energy in the backscattering process that the reflection coefficient would significantly change over subsequent reflections, which is approximately correct at very low energies.

Saturation effects may also play a role in the amount of hydrogen coming back from the walls. In metals the implanted hydrogen will change the kinetic reflection only slightly. This is not the case at low temperatures, or for the gettering metals like Ti [1]. If after some bombardment the concentration of hydrogen in the metal has reached its maximum concentration, some fraction, χ, of the implanted hydrogen will diffuse back to the surface and desorb thermally as hydrogen molecules. Therefore it may be necessary to assume in plasma edge calculations that the fraction of $(1 - R_N)\chi/2$, where $\chi \leq 1$, comes back from the surface as thermal hydrogen molecules after saturation of the target.

3. The Data Reduction Technique

For each projectile/target combination, and for each incident energy, E_o, and angle, α, experiment or computation gives a three-dimensional differential scattering distribution

$$P_{E_\circ,\alpha}(v,\beta,\phi)v^2 dv \sin\beta d\beta d\phi. \quad (1)$$

where v, β, and ϕ are the reflected velocity, polar angle, and azimuthal angle, measured from the plane of the incident trajectory, in that order (Fig. 1) [17].

We now describe an efficient method which can be conveniently used in Monte Carlo models for storing and sampling from $P_{E_\circ,\alpha}v^2 dv \sin\beta d\beta d\phi$. This method is fast and economical in storage, and does not use the rejection method for sampling from these distributions, which can be highly peaked in certain regions.

The algorithm reduces sampling from Eq. 1 to sampling three one-dimensional distributions consecutively. Assuming that the distribution $P_{E_\circ,\alpha}v^2 dv \sin\beta d\beta d\phi$ has been suitably normalized, $v_\circ$ is chosen first from

$$f^1_{E_\circ,\alpha}(v) = \int\int P_{E_\circ,\alpha}(v,\beta,\phi)\sin\beta d\beta d\phi.$$

Given $v_\circ$, $\beta_\circ$ is then picked from

$$f^2_{E_\circ,\alpha,v_\circ}(\beta) = \int P_{E_\circ,\alpha}(v_\circ,\beta,\phi)d\phi,$$

and finally, with $v_\circ$ and $\beta_\circ$ known, $\phi_\circ$ is selected from the distribution

$$f^3_{E_\circ,\alpha,v_\circ,\beta_\circ}(\phi) = P_{E_\circ,\alpha}(v_\circ,\beta_\circ,\phi).$$

The problem now reduces to sampling a one dimensional distribution f. Assuming that $\int_0^a f(y)dy = 1$, this is done by computing the inverse $\mathrm{F}(\omega) = \mathrm{G}^{-1}(\omega)$ of the cumulative distribution G of f defined by

$$G(x) = \int_0^x f(y)dy.$$

Hence a random number $\omega = G(x)$ between 0 and 1 corresponds by F to the point $x = F(\omega)$.

Suppose that $F^1_{E_\circ,\alpha}(\xi)$, $F^2_{E_\circ,\alpha}(\eta,\xi)$, and $F^3_{E_\circ,\alpha}(\varsigma,\eta,\xi)$ are the inverse cumulative distributions of $f^1_{E_\circ,\alpha}$, $f^2_{E_\circ,\alpha}$, and $f^3_{E_\circ,\alpha}$ respectively. Choose three random numbers ω_1, ω_2, and ω_3 between 0 and 1. Then the corresponding velocity of the reflected particle is $F^1_{E_\circ,\alpha}(\omega_1)$, the polar angle of reflection is $F^2_{E_\circ,\alpha}(\omega_2,\omega_1)$, and the azimuthal angle of reflection is $F^3_{E_\circ,\alpha}(\omega_3,\omega_2,\omega_1)$.

The inverse distributions F have been tabulated by storing their values for the values $\omega = 0.1$, 0.3, 0.5, 0.7, and 0.9. They may be approximated elsewhere by linear interpolation. The data for F^1, F^2, and F^3 have been calculated for hydrogen and deuterium bombardment of carbon and iron. Twelve incident energies $E_\circ$ were chosen: 1, 2, 5, 10, ...5000 eV. For each energy seven angles of incidence, α, were used: 0°, 30°, 45°, 60°, 70°, 80°, and 85°. Thus for each projectile/target combination 84 data sets were calculated.

An example data set is shown in Fig. 2 for deuterium incident on iron with $E_\circ$ = 200 eV and $\alpha = 30°$. Suppose, for example, that a reflection occurs, and that, for simplicity, the three choices of random numbers between 0 and 1 are $\omega_1 = 0.3$, $\omega_2 = 0.5$, and

$\omega_3 = 0.9$. Then using Fig. 2, the reflected energy is $F^1(2) = 91.665\,\text{eV}$, $\cos\beta = F^2(3,2) = 0.62778$, and $\cos\phi = F^3(5,3,2) = -0.30495$. (Note that it is more convenient to store the directional cosines $\cos\beta$ and $\cos\phi$ instead of β and ϕ.)

The depth distribution $D(x)$ of implanted particles is given below the distributions F^1, F^2, and F^3, in Fig. 2. The first value, $D(x = 0)$, is the fraction of incident particles which has not penetrated the solid. The energy of these particles is too low to overcome the surface binding energy, leading to an adsorption in the calculations. The next 100 values for $D(x)$ are the depth distribution, where the depth interval is given in Å by the ninth number in the first line of Fig. 2. The values of the depth distribution are per implanted particle.

In addition to the datasets, plots of the energy and angular distributions of reflected particles, and of the depth distribution of implanted particles were made. Figs. 3-6 show a complete set of these plots for the dataset shown in Fig. 2.

The energy distribution of the reflected particles is depicted in Fig. 3, together with the charges, Z_1, Z_2, and masses, M_1, M_2, of the incident particles and target atoms, the incident energy, E_o, the angle of incidence, α, and the number of Monte Carlo histories used in the calculation, NH. Fig. 3 also gives the particle reflection coefficient, R_N, the energy reflection coefficient, R_E, and the mean energy in eV, E_{mean}, of reflected particles.

The five polar angle distributions of the reduction algorithm are given in Fig. 4. The energies $E_1, \ldots, E_5$ are the energies F^1 given in line 2 of Fig. 2. The 25 azimuthal angle distributions are plotted in Fig. 5. The energies at the top are again the F^1 values from Fig. 2. The β values of each azimuthal plot are the polar angles, the cosines of which are the values of F^2 in Fig. 2. The depth distribution $D(x)$ is plotted in Fig. 6. The value $D(0)$ is not shown. The depth distribution may be used as a source term for studying the diffusion of implanted particles in the wall.

4. Applications in Transport Calculations

The data are stored at the computer centers in IPP Garching, the MFECC at Livermore, and KFA Jülich, and are available through the authors, as well as microfiche of the datasets and their corresponding figures. The sources for FORTRAN routines for reading and using the algorithm described in Section 3 are also available.

The computer storage needed for each projectile/target combination is 13020 words. This is small enough to be stored directly in a transport program, rather than on a magnetic disk, so that access to the tables during a calculation can be made very quickly.

The computational cost of using the data sets in tabular form has been compared to the cost of using fits to reflection data. An example fit to the reflection coefficient, R_N, which includes dependencies on both the incident energy, E_{in}, and polar angle, α, is given in Ref. 18, in the form:

$$R_N(E_{in}, \alpha) = 1.0 + (1.0 - \frac{\alpha}{90^\circ})[R_N^\circ(E_{in}) - 1.0], \qquad (2)$$

where

$$R_N^\circ(E_{in}) = -0.237 \log_{10}(E_{in}/E_L) + 0.19,$$

and E_L is the energy reduction constant. Comparison calculations showed that using our sampling algorithm to model reflection is, on the average, only $\sim 25\%$ slower than evaluating Eq. 2 and the analogous expression for the reflected velocity. We note that using the TRIM code directly to compute reflection was approximately 200 times slower than the sampling method. In modeling neutral transport with the DEGAS code, the overall transport calculations typically spend less than 10% of the time computing reflections. Thus there is little penalty in cost for using the sampling algorithm.

Two problems were modeled to test the sensitivity of the results to the reflection model used. One reflection model used was the one described here. The other was a simplified version of it, which omitted any angular dependence of the reflection coefficient, using only reflection coefficients for normal incidence, and which assumed a cosine dependence in the distribution in reflected polar angles.

Neutral transport was first simulated in a PLT size geometry, with a plasma radius of 40 cm and a vacuum vessel minor radius of 50 cm. Typical profiles of plasma parameters were assumed, with a central plasma temperature of 500 eV, and average density of $1.8 \times 10^{12}/\text{cm}^3$. The neutral source was due to plasma recycling at the wall. The charge-exchange power onto the wall calculated using the complete reflection model, was 14% higher than that computed using the simplified model. The reionization profile calculated with the complete model was more peaked than the one determined by the simple model. The complete model predicted that half of the neutrals reionize within a minor radius of 33.5 cm, whereas the simple model predicted this radius to be 35 cm, a 5% difference.

The second modeling problem was the calculation of the transmission probability, K, of deuterium atoms of energies from 50 to 250 eV, through a square duct. Particles of such energy might enter a pump duct of a reactor pump limiter, and their conductance through the duct is a factor in the particle removal efficiency of the pump limiter. Transmission through three ducts, 10, 40 and 100 cm in length, of 10 cm square cross-section was simulated, using the DEGAS code. The enhancement of K over the classical values from molecular flow theory [19], for incident particles of 50 eV, varied from 1.17 in the case of a 10 cm long duct, to 1.61 in the 100 cm duct. At an incident energy of 250 eV these enhancements dropped to 1.11 and 1.41, respectively, as the effect of the reflection model was weaker because the reflection coefficients were lower.

In conclusion, the algorithm for modeling wall reflection described here is a relatively efficient one, and modest in computer storage requirements. It should contribute towards more realistic calculations of neutral transport in a range of applications.

Acknowledgments

The authors would like to thank Dr. R. Behrisch for his support of our work. This work was partially supported by the U.S. Department of Energy Contract No. DE-AC02-76-CHO3073. One of the authors (W.E.) would like to thank A. Naermann for his help in the production of the data.

Figure Captions

Fig. 1. The coordinate system of the wall reflection scattering distribution.

Fig. 2. A data set for deuterium incident on Fe with $E_\circ = 200\,\text{eV}$ and $\alpha = 30°$. The first row in the set gives the atomic numbers and masses in AMU of the incident particle and target species, in that order, the incident energy and polar angle, the particle and energy reflection coefficients, the length, ℓ, of the depth division (in Å) used for the implantation distribution, and the number of Monte Carlo histories used in the TRIM calculation. The second row gives the five energy values, F^1, the next five rows give the polar angle values F^2, and the following 25 rows give the azimuthal angle values F^3. The bottom block is the implanted particle distribution, $D(x)$. The first value is the fraction of adsorbed incident atoms, $D(x = 0)$, and the following 20 rows give the implantation distribution, per implanted particle, in depth intervals of ℓ Å.

Fig. 3. The energy distribution of backscattered particles for deuterium on Fe with $E_\circ = 200\,\text{eV}$ and $\alpha = 30°$. The input data are: Z_1 = the atomic number of the incident particle, M_1 = the mass of the incident particle in AMU, Z_2 = the atomic number of the target element, M_2 = the mass of the target element in AMU, and NH = the number of Monte Carlo histories used in the TRIM calculation. The output data are: R_N, the particle reflection coefficient, R_E, the energy reflection coefficient, and E_{mean}, the mean energy in eV of backscattered particles.

Fig. 4. The distributions of the polar angles of backscattered particles for the five energy regions, for the case of deuterium on Fe with $E_\circ = 200\,\text{eV}$ and $\alpha = 30°$.

Fig. 5. The distributions of the azimuthal angles of backscattered particles, for deuterium on Fe at $E_\circ = 200\,\text{eV}$ and $\alpha = 30°$. Each of the 25 distributions belongs to one of the five energy regions given in Fig. 4, and to one of the 25 polar angle regions β. In each row the energy regions (with a mean energy E given in Fig. 4) is fixed. The values for β are the mean polar angles of the polar angle regions. The values denoted by "scale" are the maximum value for each polar graph. The positive x-axis corresponds to the azimuthal angle $\phi = 0°$.

Fig. 6. The particle implantation depth distribution, per implanted particle, for deuterium on Fe, with $E_\circ = 200\,\text{eV}$ and $\alpha = 30°$. The profile is plotted by linearly connecting the values for the populations in the depth bins, instead of in histogram form.

References

[1] R.A. Langley et al., Nucl. Fus. special issue 1984: Data Compendium for Plasma-Surface Interactions, IAEA, Vienna, 1984, and T. Tabata et al., Institute of Plasma Physics, Nagoya University, Japan Rep. IPPJ-AM-18 (1981), Rep. IPPJ-AM-34 (1984), and Rep. IPPJ-AM-41 (1985).

[2] T. Tabata et al., Appl. Phys. **20** (1981) 1929.

[3] Y. Seki et al., Nucl. Fus. **20** (1980) 1283.

[4] M.T. Robinson and J.M. Torrens, Phys. Rev. **B9** (1974) 5608.

[5] J.P. Biersack and L.G. Haggmark, NIM **174** (1880) 257.

[6] G. Bateman, Princeton Plasma Physics Laboratory Appl. Phys. Rep. No. 1 (1980).

[7] D.B. Heifetz et al., J. Comp. Phys. **46** (1982) 309.

[8] M.I. Baskes, private communication.

[9] W. Eckstein and J.P. Biersack, Appl. Phys. A **38** (1985) 123.

[10] M.T. Robinson, in "Sputtering by Particle Bombardment I, Topics in Applied Physics", R. Behrisch, Ed., Springer-Verlag, Berlin, 1981, Vol. 47, 96.

[11] O.S. Oen and M.T. Robinson, NIM **132** (1976) 647.

[12] H.H. Andersen and J.F. Ziegler, in "The Stopping and Ranges of Ions in Matter, Vol. 3." J.F. Ziegler, Ed., Pergamon Press, New York, 1977.

[13] W. Wilson et al., Phys. Rev. B **15** (1977) 2458.

[14] J. O'Connor and J.P. Biersack, NIM **B15** (1986) 14.

[15] W. Eckstein and H. Verbeek, Max-Planck-Institut für Plasmaphysik, Garching, FRG, Report No. IPP 9/32 (1979).

[16] V.M. Sotnikov, Sov. J. Plasma Phys. **7(2)** (1981) 236.

[17] D. Heifetz, in "Physics of Plasma Wall Interactions in Controlled Fusion," D. Post and R. Behrisch, Eds., Plenum Press, New York, 1986, p. 695.

[18] Y. Tokunaga et al., Comp. Phys. Comms. **38** (1985) 15-26.

[19] S. Dushman, "Scientific Foundations of Vacuum Technique," J. Wiley & Sons, New York (1962).

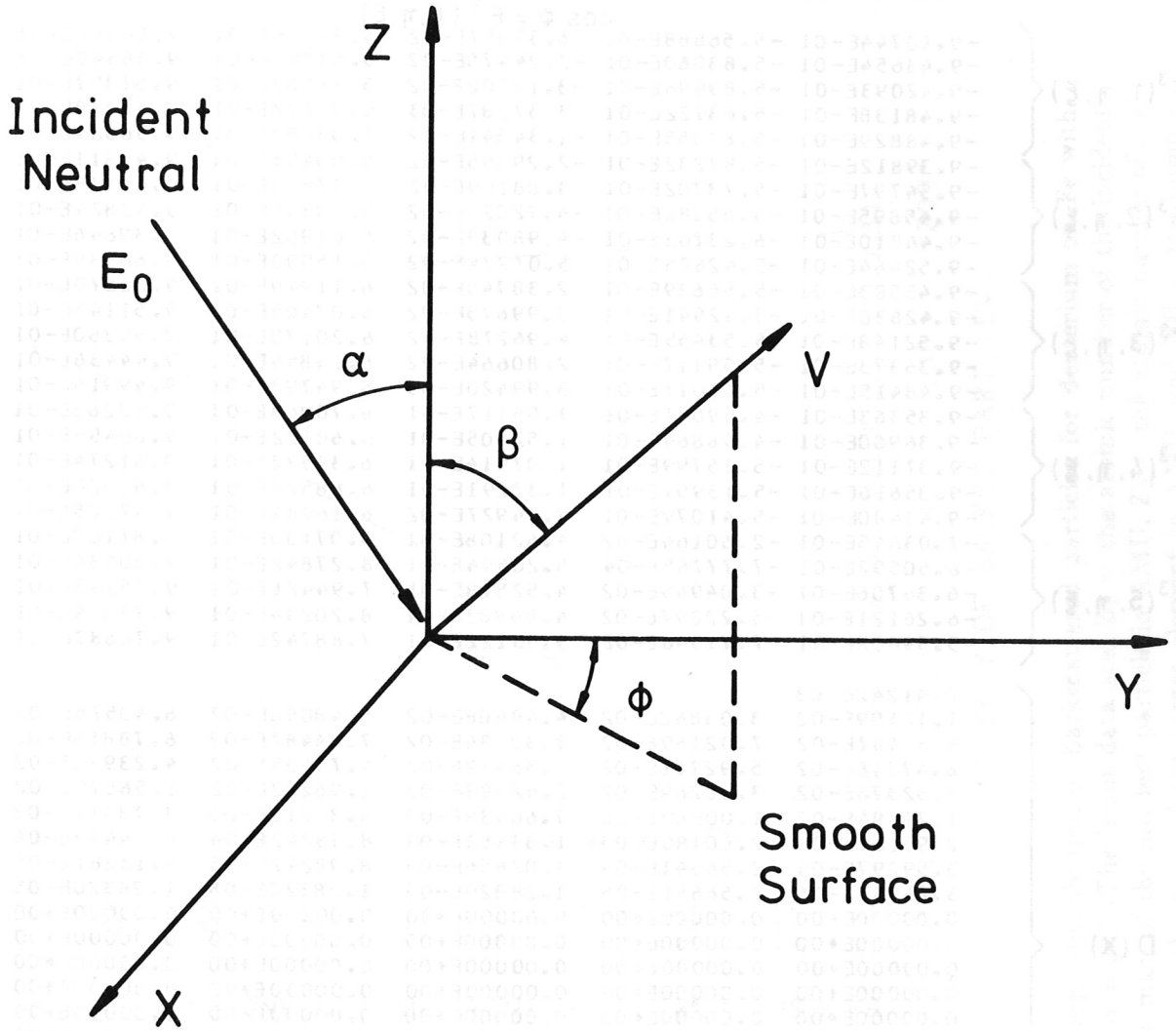

Fig. 1. The coordinate system of the wall reflection scattering distribution.

1 2.01 26 55.85 0.20E+03 30.0 0.48E+00 0.28E+00 4.0 150000

$E = F^1(\xi)$

4.11621E+01	9.16650E+01	1.25388E+02	1.50845E+02	1.72264E+02

$\cos\beta = F^2(\eta, \xi)$

4.82512E-01	6.71025E-01	7.93261E-01	8.86497E-01	9.64969E-01
4.64730E-01	6.53370E-01	7.78114E-01	8.76673E-01	9.60974E-01
4.33166E-01	6.27778E-01	7.58580E-01	8.67415E-01	9.57185E-01
4.18912E-01	6.07695E-01	7.37668E-01	8.49384E-01	9.52098E-01
3.16181E-01	4.77127E-01	6.08052E-01	7.38092E-01	8.90093E-01

$\cos\phi = F^3(\zeta, \eta, \xi)$

$F^3(1, \eta, \xi)$	-9.40744E-01	-5.56888E-01	6.39957E-02	6.32576E-01	9.56665E-01
	-9.43654E-01	-5.83060E-01	-2.24479E-02	5.53254E-01	9.38340E-01
	-9.42093E-01	-5.89996E-01	-3.12502E-02	5.86502E-01	9.51357E-01
	-9.48138E-01	-5.63722E-01	3.37287E-03	6.00102E-01	9.56278E-01
	-9.48829E-01	-5.67355E-01	-1.34341E-02	5.95892E-01	9.56689E-01
$F^3(2, \eta, \xi)$	-9.39812E-01	-5.87232E-01	-2.29355E-02	5.59451E-01	9.44811E-01
	-9.54797E-01	-5.73702E-01	3.88109E-02	5.87853E-01	9.49178E-01
	-9.45895E-01	-5.85986E-01	-4.72025E-02	5.59331E-01	9.42824E-01
	-9.46810E-01	-6.23763E-01	-4.98033E-02	5.61962E-01	9.39646E-01
	-9.52464E-01	-5.42686E-01	5.07274E-02	6.15900E-01	9.60989E-01
$F^3(3, \eta, \xi)$	-9.45583E-01	-5.56639E-01	2.38740E-02	6.11949E-01	9.62670E-01
	-9.42630E-01	-5.42541E-01	3.99673E-02	6.07405E-01	9.51145E-01
	-9.52148E-01	-5.53455E-01	4.96278E-02	6.20170E-01	9.55360E-01
	-9.36373E-01	-5.59117E-01	2.80664E-02	6.24856E-01	9.44436E-01
	-9.48415E-01	-5.61017E-01	3.99420E-03	5.94793E-01	9.49916E-01
$F^3(4, \eta, \xi)$	-9.35363E-01	-4.59087E-01	1.55117E-01	6.70963E-01	9.52263E-01
	-9.36900E-01	-4.98864E-01	1.52805E-01	6.60322E-01	9.60455E-01
	-9.37112E-01	-5.15799E-01	1.07914E-01	6.31572E-01	9.61274E-01
	-9.35616E-01	-5.13909E-01	1.37291E-01	6.88522E-01	9.63320E-01
	-9.43480E-01	-5.41079E-01	7.34927E-02	6.16984E-01	9.47225E-01
$F^3(5, \eta, \xi)$	-7.03645E-01	-2.60166E-02	4.62108E-01	8.07130E-01	9.81169E-01
	-6.50592E-01	-7.77765E-04	5.20594E-01	8.27842E-01	9.80434E-01
	-6.36706E-01	-3.04945E-02	4.52518E-01	7.94421E-01	9.75293E-01
	-6.26121E-01	-5.22297E-02	4.84883E-01	8.20234E-01	9.78384E-01
	-5.59808E-01	-7.71548E-02	3.96122E-01	7.88742E-01	9.76687E-01

D(X)	2.41242E-03				
	1.12409E-02	3.03862E-02	4.48608E-02	5.48056E-02	6.40575E-02
	6.85487E-02	7.02169E-02	7.30784E-02	7.14487E-02	6.78814E-02
	6.47248E-02	5.92711E-02	5.38432E-02	4.79405E-02	4.23970E-02
	3.62376E-02	3.00269E-02	2.42397E-02	1.96202E-02	1.56679E-02
	1.27294E-02	1.00860E-02	7.60939E-03	5.33812E-03	3.73412E-03
	2.95137E-03	2.00180E-03	1.33453E-03	8.98242E-04	6.54433E-04
	3.59297E-04	2.56641E-04	1.02656E-04	8.98242E-05	5.13281E-05
	3.84961E-05	2.56641E-05	1.28320E-05	1.28320E-05	1.28320E-05
	0.00000E+00	0.00000E+00	0.00000E+00	0.00000E+00	0.00000E+00
	0.00000E+00	0.00000E+00	0.00000E+00	0.00000E+00	0.00000E+00
	0.00000E+00	0.00000E+00	0.00000E+00	0.00000E+00	0.00000E+00
	0.00000E+00	0.00000E+00	0.00000E+00	0.00000E+00	0.00000E+00
	0.00000E+00	0.00000E+00	0.00000E+00	0.00000E+00	0.00000E+00
	0.00000E+00	0.00000E+00	0.00000E+00	0.00000E+00	0.00000E+00
	0.00000E+00	0.00000E+00	0.00000E+00	0.00000E+00	0.00000E+00
	0.00000E+00	0.00000E+00	0.00000E+00	0.00000E+00	0.00000E+00
	0.00000E+00	0.00000E+00	0.00000E+00	0.00000E+00	0.00000E+00
	0.00000E+00	0.00000E+00	0.00000E+00	0.00000E+00	0.00000E+00
	0.00000E+00	0.00000E+00	0.00000E+00	0.00000E+00	0.00000E+00
	0.00000E+00	0.00000E+00	0.00000E+00	0.00000E+00	0.00000E+00

Fig. 2. A data set for deuterium incident on Fe with $E_\circ = 200\,\mathrm{eV}$ and $\alpha = 30°$. The first row in the set gives the atomic numbers and masses in AMU of the incident particle and target species, in that order, the incident energy and polar angle, the particle and energy reflection coefficients, the length, ℓ, of the depth division (in Å) used for the implantation distribution, and the number of Monte Carlo histories used in the TRIM calculation. The second row gives the five energy values, F^1, the next five rows give the polar angle values F^2, and the following 25 rows give the azimuthal angle values F^3. The bottom block is the implanted particle distribution, $D(x)$. The first value is the fraction of adsorbed incident atoms, $D(x = 0)$, and the following 20 rows give the implantation distribution, per implanted particle, in depth intervals of ℓ Å.

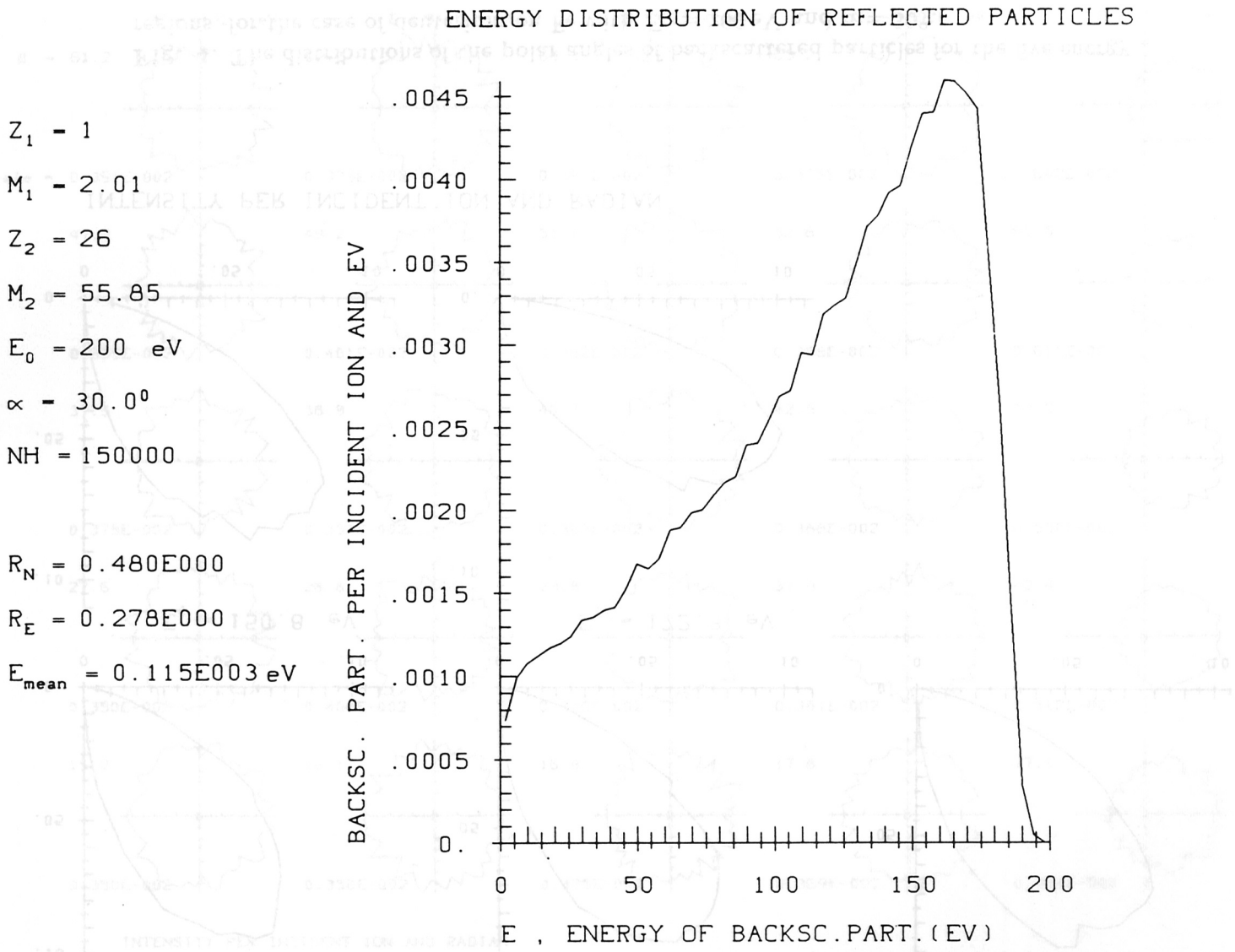

Fig. 3. The energy distribution of backscattered particles for deuterium on Fe with $E_\circ = 200\,\text{eV}$ and $\alpha = 30°$. The input data are: Z_1 = the atomic number of the incident particle, M_1 = the mass of the incident particle in AMU, Z_2 = the atomic number of the target element, M_2 = the mass of the target element in AMU, and NH = the number of Monte Carlo histories used in the TRIM calculation. The output data are: R_N, the particle reflection coefficient, R_E, the energy reflection coefficient, and E_{mean}, the mean energy in eV of backscattered particles.

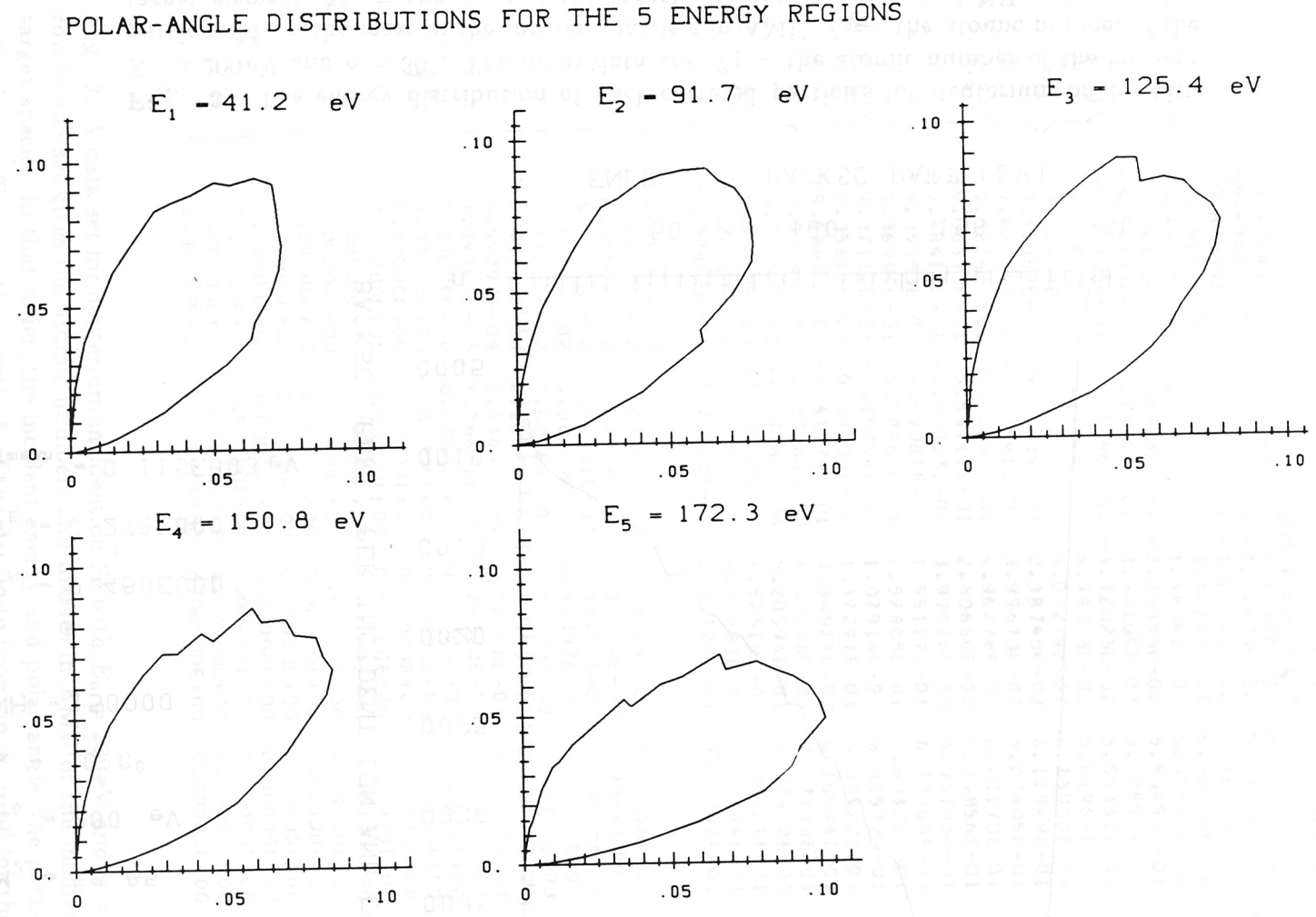

Fig. 4. The distributions of the polar angles of backscattered particles for the five energy regions, for the case of deuterium on Fe with $E_\circ = 200\,\mathrm{eV}$ and $\alpha = 30°$.

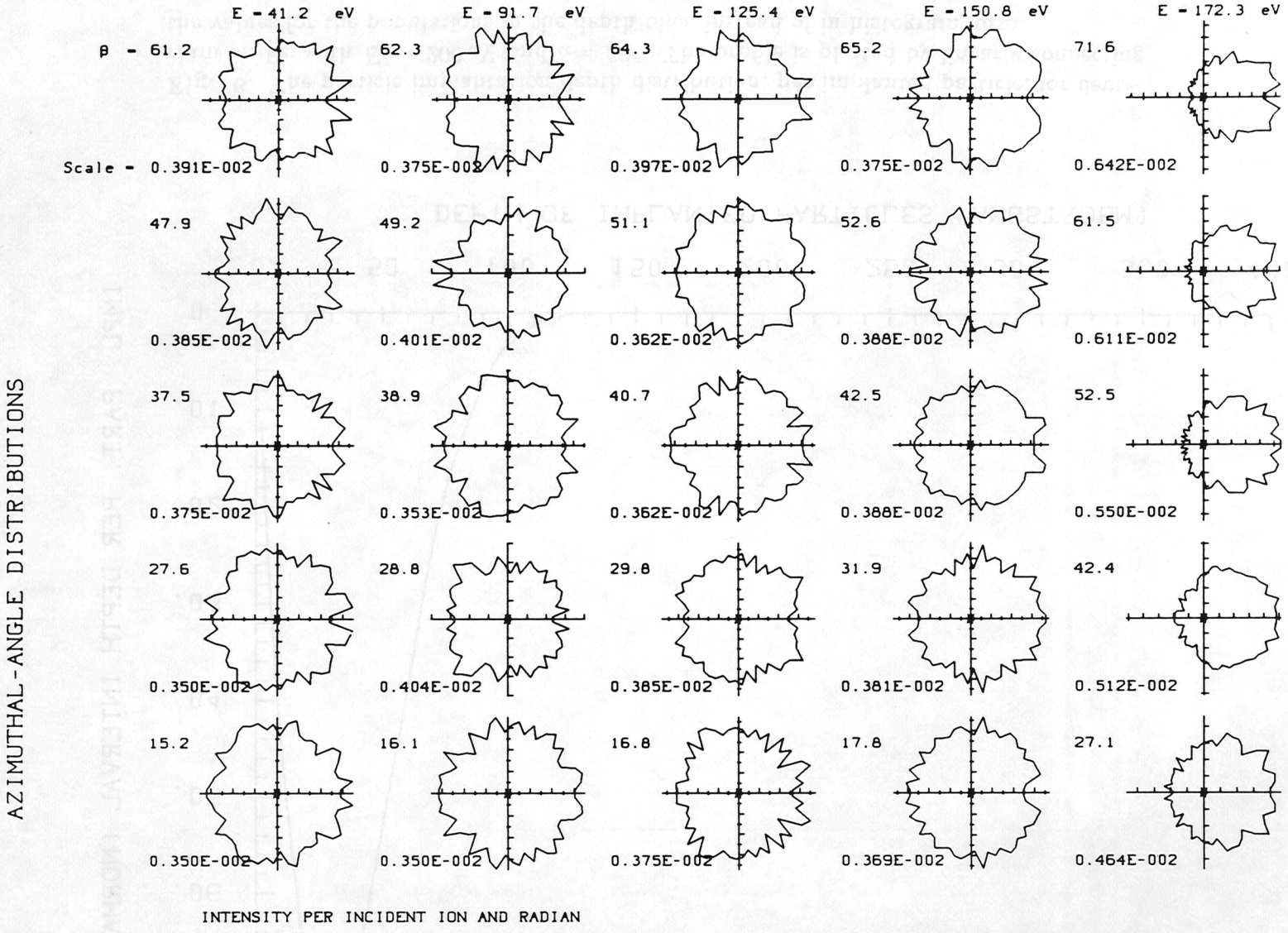

Fig. 5. The distributions of the azimuthal angles of backscattered particles, for deuterium on Fe at $E_\circ = 200\,\mathrm{eV}$ and $\alpha = 30°$. Each of the 25 distributions belongs to one of the five energy regions given in Fig. 4, and to one of the 25 polar angle regions β. In each row the energy regions (with a mean energy E given in Fig. 4) is fixed. The values for β are the mean polar angles of the polar angle regions. The values denoted by "scale" are the maximum value for each polar graph. The positive x-axis corresponds to the azimuthal angle $\phi = 0°$.

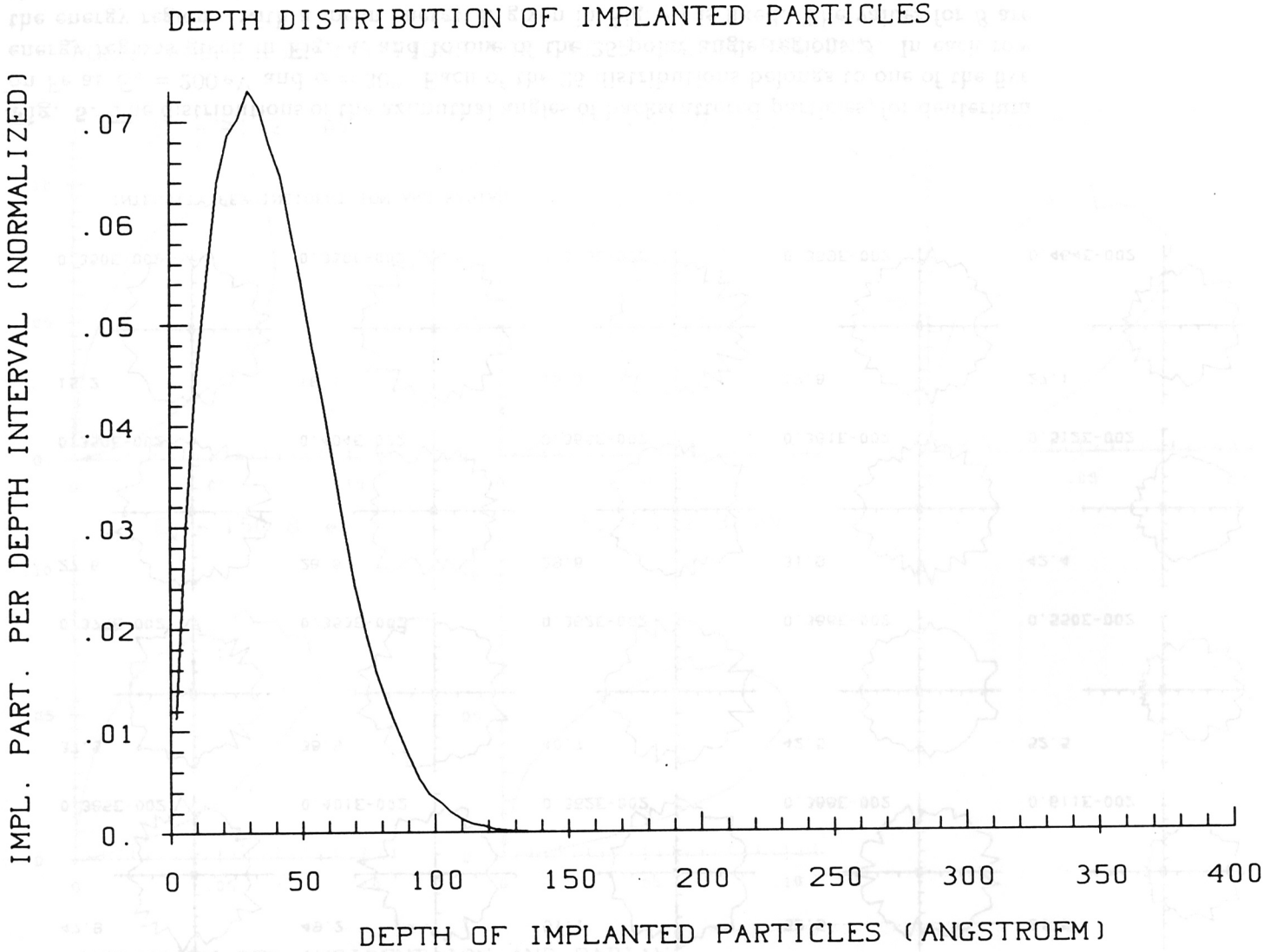

Fig. 6. The particle implantation depth distribution, per implanted particle, for deuterium on Fe, with $E_c = 200\,\mathrm{eV}$ and $\alpha = 30°$. The profile is plotted by linearly connecting the values for the populations in the depth bins, instead of in histogram form.